

Electron-phonon coupling in n -type Ge two-dimensional systemsC. Ciano,¹ L. Persichetti^{1,*}, M. Montanari¹, L. Di Gaspare¹, G. Capellini,^{1,2} L. Baldassarre,³ M. Ortolani,³ A. Pashkin,⁴ M. Helm,^{4,5} S. Winnerl,⁴ M. Virgilio,^{6,†} and M. De Seta^{1,‡}¹*Dipartimento di Scienze, Università degli Studi Roma Tre, Viale G. Marconi 446, I-00146, Roma, Italy*²*IHP – Leibniz-Institut für innovative Mikroelektronik, Im Technologiepark 25, D-15236 Frankfurt (Oder), Germany*³*Dipartimento di Fisica, Università di Roma Sapienza, Piazzale A. Moro 2, I-00185 Rome, Italy*⁴*Institute of Ion Beam Physics and Materials Research, Helmholtz-Zentrum Dresden-Rossendorf, Bautzner Landstrasse 400, D-01328 Dresden, Germany*⁵*Institut für Angewandte Physik, TU Dresden, D-01062 Dresden, Germany*⁶*Dipartimento di Fisica “E. Fermi,” Università di Pisa, Largo Pontecorvo 3, I-56127 Pisa, Italy*

(Received 31 August 2020; accepted 27 October 2020; published 16 November 2020)

Electron-optical phonon interaction is the dominant energy-loss mechanism in low-dimensional Ge/SiGe heterostructures and represents a key parameter for the design and realization of electronic and optoelectronic devices based on this material system compatible with the mainstream Si complementary metal-oxide semiconductor technology. Here we investigate the intersubband relaxation dynamics of n -type Ge/SiGe multi-quantum wells with different symmetry and design by means of single-color pump-probe spectroscopy. By comparing the experimental differential transmittance data as a function of the pump-probe delay with numerical calculations based on an energy-balance rate-equation model, we could quantify an effective value for the optical phonon deformation potential describing the electron-phonon coupling in two-dimensional Ge-based systems. We found nonradiative relaxation times longer than 20 ps even in samples having intersubband energy separations larger than the optical phonon energy, evidencing the presence of a less effective electron-phonon coupling with respect to that estimated in bulk Ge.

DOI: [10.1103/PhysRevB.102.205302](https://doi.org/10.1103/PhysRevB.102.205302)**I. INTRODUCTION**

Carrier scattering in low-dimensional systems is characterized by peculiar features with respect to bulk materials. On one side, this is due to the deep modifications of the electronic spectrum induced by the reduced dimensionality and by the emerging of subbands with associated confined wave functions. On the other side, the unavoidable presence of interface roughness (IFR) introduces a scattering mechanism, first addressed in Ref. [1], which is absent in bulk semiconductors.

Due to a more mature epitaxy technology, carrier scattering in low-dimensional systems has been investigated mainly focusing on III-V-based structures [2,3]. However, in the last two decades, advances in group-IV epitaxy have made it possible to grow SiGe multilayer systems with high crystal quality [4–8]; consequently, this class of materials is attracting increasing research efforts, mainly motivated by its prompt integrability with the mainstream complementary metal-oxide semiconductor standard. In particular, in the last 10 years, Ge-rich SiGe structures have been actively investigated, and applications have been proposed in different contexts as for instance quantum computing [8–10], Si-based photonics [11–13], high-mobility transistors [14,15], and thermoelec-

tricity [16,17]. The recently demonstrated [18] incorporation of Sn to obtain Ge-rich ternary SiGeSn alloys has further enlarged the design flexibility of this material system.

When addressing the carrier scattering rates in indirect-gap Ge-rich alloys, the degeneracy of the conduction-band minima associated with the L point and the nonpolar character of their lattice represent the most remarkable differences with respect to III-V systems. In this paper, we focus on the electron-phonon coupling which controls the inelastic scattering of electrons with the optical phonon (OP) branch in n -type Ge-rich two-dimensional (2D) multilayers. This study is motivated by the absence of accurate literature data, despite the electron-OP interaction is being the dominant energy-loss mechanism [19], and crucially contributes to many other physical phenomena, such as free-carrier absorption, Raman scattering, or excited level lifetimes [20]. To this regard, we note that, due to the absence of the Fröhlich interaction in nonpolar lattices, the electron-OP coupling is controlled by the deformation potential, and therefore lower scattering rates are generally expected. This feature opens the possibility to extend toward higher values the temperature operation range of quantum devices, as for instance the THz quantum cascade lasers [13].

In contrast to the deformation potential associated with acoustic excitations, which can be easily probed by electron or hole transport measurements at low temperature and low field or from the variation of the optical properties caused by an applied lattice strain field [21], the evaluation of the deformation potential associated with OPs is more elusive

*luca.persichetti@uniroma3.it

†michele.virgilio@unipi.it

‡monica.deseta@uniroma3.it

TABLE I. Sample parameters. w is the thickness of the Ge well; in brackets the thickness of the $\text{Si}_{0.03}\text{Ge}_{0.97}$ step layer for the stepwise configuration. n_{2D} is the sheet carrier density evaluated from optical absorption spectra. E_{12} is the L_1 - L_2 ISB transition energy obtained from SP calculations. $E_{12,\text{abs}}$ is the energy of the L_1 - L_2 optical resonance; unbracketed (bracketed) values are obtained from experiments (SP calculations including depolarization shift). $\hbar\omega^{\text{FEL}}$ is the FEL pump (probe) photon energy.

Sample details						
Sample	MQW Design	Thickness w Ge well (thickness step layer) (nm)	n_{2D} ($\times 10^{11} \text{ cm}^{-2}$)	E_{12} (meV)	$E_{12,\text{abs}}$ (meV)	$\hbar\omega^{\text{FEL}}$ (meV)
S1	Symmetric	24.0	1.5 ^a	11.8	16.2 (15.0)	14.1
S2	Stepwise	11.5 (13.0)	2.5	19.7	23.0 (22.6)	23.5
S3	Symmetric	18.0	1.2	23.6	27.5 (25.4)	27.0
S4	Symmetric	14.0	1.1 ^a	27.4	28.4(29.2)	28.8
S5	Symmetric	12.0	1.0 ^a	35.9	37.0 (37.0)	40.7
S6	Symmetric	12.0	1.0	36.1	39.0 (37.6)	40.7
S7	Symmetric	10.0	1.0	46.2	46.5 (46.3)	46.0

^aModulation doping by phosphine codeposition in the $\text{Si}_{0.20}\text{Ge}_{0.80}$ barriers.

[22]. This is due to the fact that, while the strain deforms the unit cell as a whole, OP excitations are associated with oscillations of the relative displacement of the ions located within the same unit cell. In addition, a precise evaluation of the electron-OP interaction through transport measurements suffers from the simultaneous presence of both intra- and intervalley scattering processes, i.e., transitions which occur within the same or between different L valleys [23]. Nevertheless, in Refs. [24,25], effective values for the inter- and intravalley OP deformation potentials in Ge have been proposed by leveraging on Monte Carlo simulations calibrated against experimental data for the drift velocity and the diffusivity constants, acquired on bulk samples. Fully theoretical evaluations of the OP deformation potential in Ge have been also reported in literature [19,26,27]. Unfortunately, all the proposed values are quite scattered and have been obtained by means of indirect methods, therefore hindering a precise and reliable assessment of these two material parameters. Furthermore, since these studies refer to bulk crystals, the proposed values of the deformation potentials may be inappropriate to describe the interaction of OPs with 2D electrons, as noticed in Ref. [28].

To circumvent this limitation, here we propose a different approach for the measurement of the interaction between electrons and the OP phonon branch in 2D Ge-based multilayers. To this aim, we performed resonant single-color pump-probe spectroscopy experiments on n -type Ge/SiGe multiquantum wells (MQWs) samples. The decay dynamics of the differential transmission signal allowed us to probe the excited subband level population as a function of the pump-probe delay. These measurements have been compared with numerical data produced by a model which simulates the intersubband (ISB) carrier relaxation dynamics, taking into account the main nonradiative scattering mechanisms. By investigating different sample geometries and Ge well thicknesses, in order to vary the subband energy spacing across the optical phonon energy, we were able to precisely isolate the electron-OP contribution from the other scattering channels. Using the relative coupling constants as fitting parameters, a very good match with experimental data has been obtained over a quite large set of conditions, such as different QW geometry, doping

distribution, lattice temperature, and pumping intensity. In this way, we could quantify an effective value for the OP deformation potential describing the electron-phonon coupling in 2D Ge-based systems. Our results suggest that this interaction is significantly weaker in comparison with what expected for bulk materials.

II. EXPERIMENTAL AND THEORETICAL METHODS

n -type Ge/SiGe MQW samples were grown by ultrahigh-vacuum chemical vapor deposition at 500 °C on Si(001) using ultrapure germane and silane without carrier gases. Our samples consist of a stack of 20 strain-compensated QWs deposited on a reverse step-graded virtual substrate as detailed in Ref. [7]. Six samples feature a symmetric QW geometry with a Ge well with varying thickness w , and a 21-nm-thick $\text{Si}_{0.20}\text{Ge}_{0.80}$ barrier (see Table I). In addition, one sample has been designed with a stepwise profile, consisting of a Ge well, a $\text{Si}_{0.03}\text{Ge}_{0.97}$ step, and a $\text{Si}_{0.20}\text{Ge}_{0.80}$ barrier with thicknesses of 11.5, 13 and 21 nm, respectively. To populate the fundamental subband L_1 , the well region (S2, S3, S6, S7) or alternatively the $\text{Si}_{0.20}\text{Ge}_{0.80}$ barriers (S1, S4, S5) have been codoped with phosphine.

Structural investigation of the grown samples, performed by high-resolution x-ray diffraction and scanning transmission electron microscopy, revealed high crystal quality, very sharp and flat interfaces, and a very good layer thickness and composition reproducibility along the entire stack [7,29,30]. Moreover, to accurately describe the scattering rate associated with IFR, selected samples have been investigated also by means of atom probe tomography [5]. In this way, we were able to precisely measure the root-mean square (rms) amplitude Δ (0.18 nm) and the in-plane correlation length Λ_{\parallel} (6.9 nm) associated with the interface roughness. Since it was recently demonstrated that also the roughness correlation length along the growth direction Λ_{\perp} plays a role in determining the IFR scattering rate [5], we also measured this parameter, obtaining a value of 0.26 nm. Indeed, in Ref. [5] the IFR scattering model proposed by Ando [31] has been generalized to take into account both the atom interdiffusion across the heterointerface and the correlation length along

the growth direction. When Λ_{\perp} is smaller than the interface width, as it happens for our samples, it turns out that the IFR scattering rate is reduced with respect to the abrupt interface case by a factor $F < 1$ which depends on the ratio between the interface width and Λ_{\perp} [5]. In our samples, using the measured value of 1.1 nm for the interface width we get $F = 0.35$, meaning that the rate is suppressed by a factor of 3.

To couple ISB transitions with the radiation field, a gold film was evaporated on the top surface of the samples shaped in a 70° single-pass waveguide to maximize the TM-polarized component (parallel to the growth direction) in the QW region. Preliminary to pump-probe experiments, the energies of the ISB absorption resonances have been measured by means of Fourier transform infrared (FTIR) spectroscopy (Table I) which revealed clearly distinguishable ISB signatures in the $\alpha_{2D}(\omega)$ absorption spectrum. From the intensity of the ISB features, the sheet carrier density n_{2D} has been also evaluated (Table I).

Pump-probe experiments were performed with a pulsed (half-width at half-maximum 5 ps) free-electron laser (FEL) source at the FELBE facility using a liquid-He bolometer as a detector. The frequency of the TM-polarized electric field of the FEL pump-pulse $\hbar\omega^{\text{FEL}}$ centered at $t = 0$ was tuned to excite the $L_1 \rightarrow L_2$ ISB transition (see Table I) and the transmittance $T(t)$ has been measured by means of a degenerate probe pulse as a function of the pump/probe delay time. In this way, we recorded the time evolution of the relative differential transmission, defined as $\Delta T/T_0 = [T(t) - T_0]/T_0$, where T_0 is the equilibrium transmittance, at different lattice temperatures and excitation intensities.

To model the relaxation dynamics, we first calculated electronic subband states and optical equilibrium properties by means of a self-consistent multivalley effective mass model, implemented to solve the Schrödinger-Poisson (SP) equation in SiGe multilayer systems [6]. The relaxation process was simulated using a self-consistent rate-equation approach which tracks energy and particle fluxes among different subbands [32]. From the temporal evolution of the subband populations, the relative differential transmission signal $\Delta T(t)/T_0$ was derived as detailed in Ref. [33]. In the model, the energy and particle exchange rates are calculated considering time- and subband-dependent electronic temperatures and chemical potentials. We have taken into account both elastic interactions due to the electron-electron (ee), ionized impurity (II), and IFR perturbative potentials, as well as inelastic events associated with the photon and phonon fields [32]. In this latter case, acoustic and OP branches have been included. We notice that, among all the perturbing potentials present in the model, only OP scattering events can couple initial and final states belonging to different degenerate L valleys (intervalley scattering) since the amplitude of the matrix elements associated with the other channels rapidly decays with the modulus of the exchanged momentum. L - Δ_2 scattering processes, which are expected to influence the carrier dynamics to a minor extent [34,35], have been neglected.

III. RESULTS AND DISCUSSION

As mentioned in the Introduction, the coupling of the electronic degree of freedom with the OP branch has been

modeled for bulk materials in Refs. [24,25], introducing two effective phonon energies $\hbar\omega_{\text{eff}}$ and their associated deformation potentials for intra- and intervalley scattering processes, which involve lattice excitations with small and large momentum, respectively. The effective phonon energies and coupling potentials describe the total scattering rate resulting from the joint action of both transverse and longitudinal optical phonon branches [25,36]. Following Ref. [24], we set for the intravalley (intervalley) phonon energy $\hbar\omega_{\text{eff}} = 37.1$ (27.5) meV. The relative deformation potentials are here treated as fitting parameters tuned to reproduce the measured differential transmission data. We start this fitting procedure from the values derived by Jacoboni *et al.* [24], who estimated for the intervalley $\Xi_{\text{OP}}^{\text{inter}}$ and intravalley $\Xi_{\text{OP}}^{\text{intra}}$ deformation potential the values of 3.0×10^8 and 5.5×10^8 eV/cm, respectively.

To put on a more solid basis our evaluation of the electron-OP coupling in 2D Ge/SiGe multilayer systems, we have first studied two QW structures featuring the L_1 - L_2 transition energy below both the phonon energies (S1, S2 in Table I). The rationale for this choice is that in this case the depopulation of the L_2 subband via phonon emission is suppressed. In fact, only thermally excited L_2 carriers have sufficient energy to emit an optical phonon when relaxing into the L_1 subband but electron heating effects for S1 and S2 in our experimental conditions are expected to be modest, as discussed hereinafter. Similarly, scattering processes involving the absorption of OPs are negligible due to the low lattice temperature. It follows that the intersubband dynamics at short delay times should be mainly dominated by the elastic channels. Therefore, S1 and S2 can serve as a test platform for the modeling of these scattering rates before starting the fitting procedure used to estimate those associated with the inelastic interactions. Our results for S1 and S2 are summarized in Fig. 1. In the top panels, we show the band-edge profile and the L -point envelope functions for S1 [single-symmetric QW, panel (a)] and S2 [stepwise QW, panel (b)]. The associated FTIR absorption spectra α_{2D} are reported in the central panels, and clearly show the signature of the L_1 - L_2 transition. Notice that in the S2 absorption spectrum, the high-energy shoulder of the main absorption peak is to be attributed to the L_1 - L_3 transition which is also active due to the spatial asymmetry of this QW structure. Differential transmission data acquired at low lattice temperature ($T_L = 4$ K) are shown in the bottom panels (red dots). Fitting the S1 $\Delta T/T_0$ signal with a single exponential function we obtain a decay time constant τ of (27 ± 1) ps. The corresponding value for S2 decreases down to (20 ± 6) ps, because of larger elastic intersubband rates, induced by the presence of an extra interface and a larger value of n_{2D} which enhances the Coulomb scattering channels.

Numerical differential transmission data shown in the bottom panels have been calculated adjusting the input power density in the QW region to reproduce the measured maximum for $\Delta T/T_0$, obtaining 900 and 190 W/cm² for S1 and S2, respectively. Simulations shown in Fig. 1 have been performed under different conditions: (1) taking into account all the elastic scattering channels and using the deformation potentials provided in Ref. [24] (black curve); (2) switching off all the elastic channels and adopting the values for the deformation potentials provided in Ref. [24] (magenta curve); (3) keeping active only the elastic scattering (cyan curve);

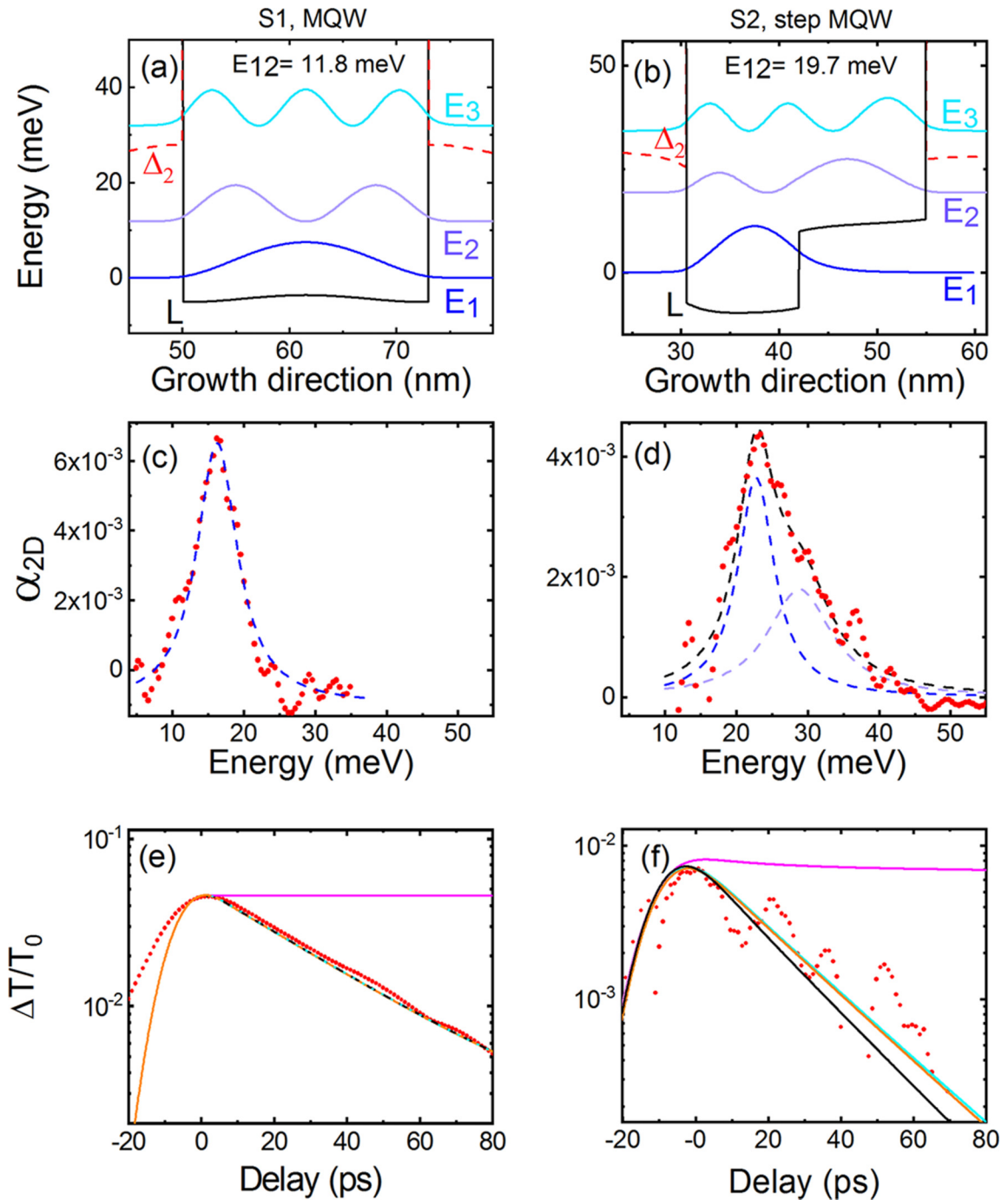


FIG. 1. (a), (b) Band-edge profiles, calculated electron energies, and squared envelope wave functions for the symmetric MQW S1 and the stepwise structure S2, respectively. The solid black and dashed red curves represent the L and Δ_2 band profiles, respectively. The theoretical energy values corresponding to the L_1 - L_2 transition are also indicated. (c), (d) The corresponding experimental ISB absorption spectra measured by FTIR (red dots). The Lorentzian fits of the resonances centered at $E_{12,abs}$ (dashed blue curve) and $E_{13,abs}$ (dashed violet curve) are displayed. For S2, the dashed black curve is the sum of the blue and violet fit curves. (e), (f) The time-resolved pump-probe signals as defined in the text for (e) S1 and (f) S2, recorded at a lattice temperature $T_L = 4$ K. The red dots are the experimental relative differential transmission data. Theoretical results for the dynamics of the relative differential transmission are reported for different sets of the material parameters driving the electron-phonon scattering: taking into account all the elastic scattering channels and using the deformation potentials provided in Ref. [24] (black curve); switching off all the elastic channels and adopting the values for the deformation potentials provided in Ref. [24] (magenta curve); keeping active only the elastic scattering (cyan curve); considering all the scattering channels but using our best-fit values for the deformation potentials as discussed in the text (orange curve).

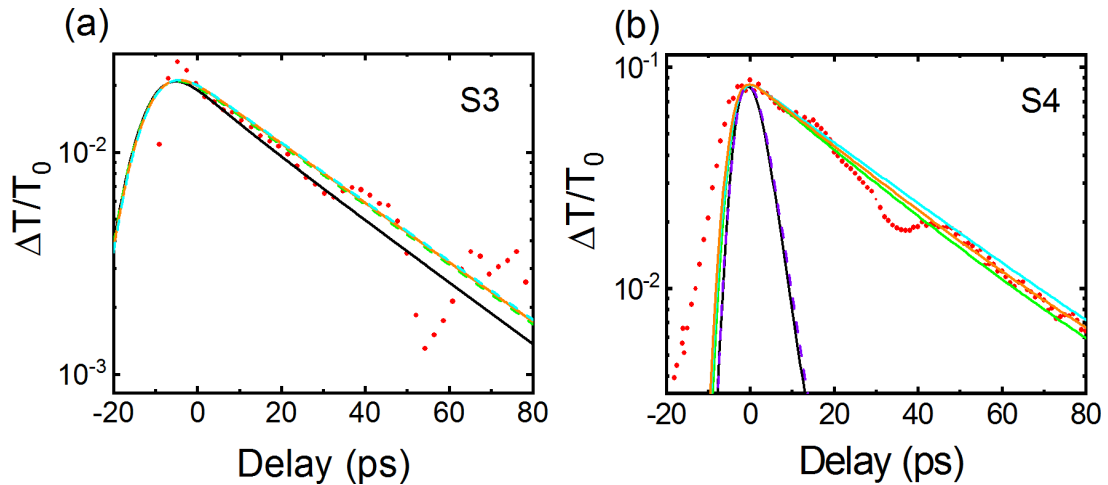


FIG. 2. Differential transmission data for sample S3 and S4 at a lattice temperature $T_L = 4$ K. The experimental curve is shown as red dots. Theoretical results for the dynamics of the relative differential transmission are reported for different sets of the material parameters driving the electron-phonon scattering: taking into account all the elastic scattering channels and using the deformation potentials provided in Ref. [24] (black curve); keeping active only the elastic scattering (cyan curve); taking into account all the elastic scattering channels, switching off the intervalley OP channel, and using the intravalley deformation potentials of Ref. [24] (green curve); considering all the scattering channels but using our best-fit values for the deformation potentials as discussed in the text (orange curve); for sample S4, taking into account all the elastic scattering channels, switching off the intravalley OP channel, and using the intervalley deformation potential of Ref. [24] (dashed purple curve).

(4) considering all the scattering channels but using our best-fit values for the deformation potentials as derived in the following (orange curve). As expected, when the elastic channels are artificially suppressed, numerical data largely overestimate the characteristic time ($t \geq 230$ ps), confirming that the OP interaction is not the dominant relaxation mechanism for S1 and S2. In line with this consideration, we find quite similar $\Delta T/T_0$ curves upon varying the OP coupling strength. In particular, the role of OPs in S1 is found to be completely negligible due to the smaller subband energy separation featured by this sample. In fact, our model indicates that for sample S1 there are almost no L_2 electrons with kinetic energy sufficient to relax into the fundamental subband via OP emission in an intervalley event. Similarly, for S2 these carriers represent less than 7% of the total L_2 population. Notice that this holds despite the high degree of optical excitation achieved in our experimental conditions. In fact the peak fraction of carriers that has been transferred into the first excited subband by the pump beam in S1 and in S2 are estimated to be as large as 15 and 2%, respectively. The good match between the experimental data and the black, orange, and cyan curves reported in Fig. 1 has been obtained also for another symmetric MQW sample (S3) which features an L_1 - L_2 transition energy comparable to the one of S2 and the same doping density of S1 [see Fig. 2(a)]. Considering that S1, S2, and S3 are characterized by dissimilar scattering rates associated with each individual elastic channel, because of the different carrier densities and number of interfaces, the good match obtained between the numerical and experimental data demonstrates that our model appropriately describes the effect of the elastic interactions. This represents a fundamental prerequisite for the validation of the fitting procedure adopted in the following to estimate the OP deformation potentials.

As a first step toward this objective, we compare in Fig. 2(b) measured and simulated $\Delta T/T_0$ curves for S4, a

symmetric MQW sample featuring a bare L_1 - L_2 transition energy at 27.4 meV, i.e., matching the OP energy associated with intervalley scattering events and well below the intravalley phonon threshold. For S4, we would expect the relaxation dynamics to be more affected by the electron-OP coupling, in particular for what concerns the intervalley processes. As a matter of fact, our simulations find very different behaviors when the inelastic interaction is turned off as apparent from the comparison of the black curve with the cyan one [see Fig. 2(b)]. However, using the deformation potentials provided in Ref. [24], the relaxation rate results to be largely overestimated with respect to the experimental data suggesting that, as proposed in Ref. [28], intervalley scattering events in Ge/SiGe 2D structures are negligible. This is apparent by comparing the measured $\Delta T/T_0$ with their numerical counterpart, obtained setting $\Xi_{\text{OP}}^{\text{inter}} = 0$ and using for $\Xi_{\text{OP}}^{\text{intra}}$ the value provided in Ref. [24] (green curve) or our best-fit value, estimated as discussed in the following (orange curve). Nevertheless, this sample cannot be used to extract a precise fit value for $\Xi_{\text{OP}}^{\text{intra}}$. In fact, despite the quite high pumping power used in the experiment, intravalley OP events still play a minor role in controlling the total relaxation rate, since the L_1 - L_2 transition energy remains quite far from the phonon threshold associated with intravalley events, as evident by the similar behavior featured by the black and the dashed purple curve, the latter obtained setting $\Xi_{\text{OP}}^{\text{intra}} = 0$.

Given the above results, it is reasonable to assume $\Xi_{\text{OP}}^{\text{inter}} = 0$ while $\Xi_{\text{OP}}^{\text{intra}}$ can be treated as the only free parameter. To determine its value, we have tuned $\Xi_{\text{OP}}^{\text{intra}}$ to fit a large set of experimental $\Delta T/T_0$ data, acquired from samples with larger L_1 - L_2 transition energies (S5, S6, and S7), which lie within the 35.9–46.2 meV range, corresponding to absorption resonances in the 37.0–46.5 meV range. The relative FTIR absorption spectra $\alpha_{2\text{D}}$ are reported in the left panels of Fig. 3. In this way, we were able to monitor the relaxation dynamics

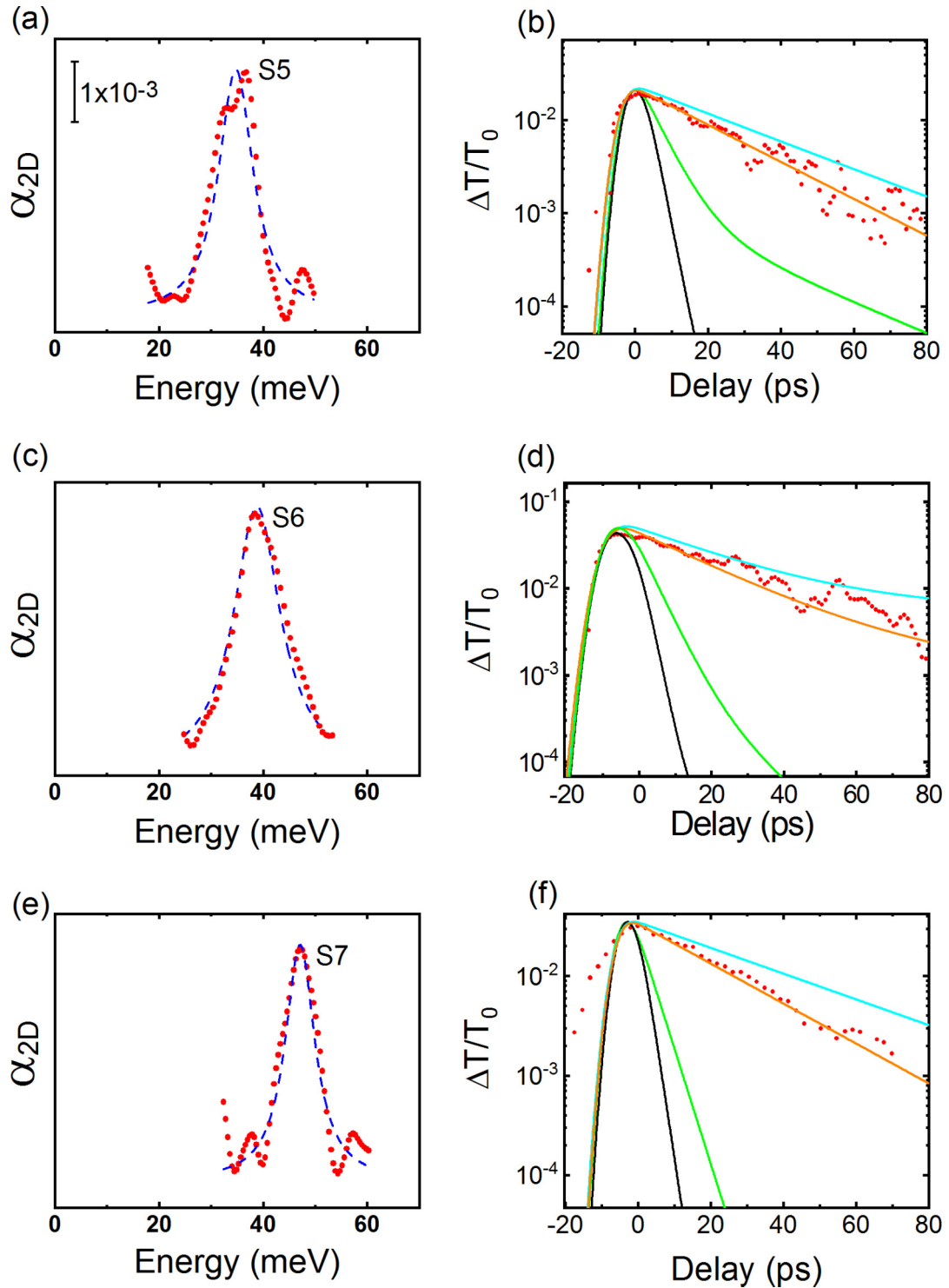


FIG. 3. (left panels) The experimental ISB absorption spectra measured by FTIR (red dots) on symmetric MQWs (a) S5, (c) S6, and (e) S7. The dashed blue curve is a Lorentzian fit to the data. (Right panels) The corresponding time-resolved pump-probe signals, recorded at a lattice temperature $T_L = 4$ K. The red dots are the experimental relative differential transmission data. Theoretical results for the dynamics of the relative differential transmission are reported for different sets of the material parameters driving the electron-phonon scattering: taking into account all the elastic scattering channels and using the deformation potentials provided in Ref. [24] (black curve); keeping active only the elastic scattering (cyan curve); taking into account all the elastic scattering channels, switching off the intervalley OP channel, and using the intravalley deformation potentials of Ref. [24] (green curve); considering all the scattering channels but using our best-fit values for the deformation potentials as discussed in the text (orange curve).

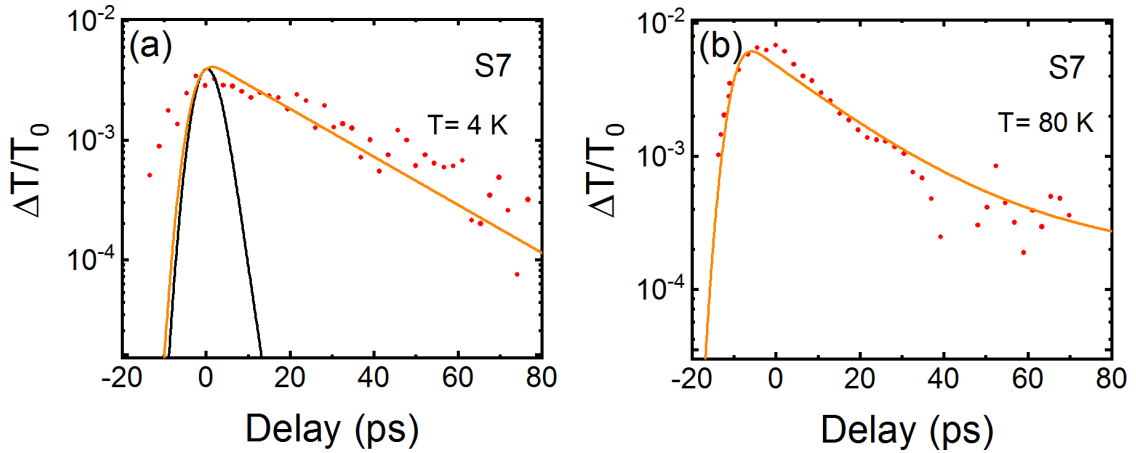


FIG. 4. The time-resolved pump-probe signals for sample S7, to be compared to Fig. 3(f). (a) Signal recorded at lower pump power (one order of magnitude less carrier is excited into L_2). (b) Signal recorded at higher lattice temperature ($T_L = 80$ K). The red dots are the experimental relative differential transmission data. Theoretical results for the dynamics of the relative differential transmission are reported for different sets of the material parameters driving the electron-phonon scattering: taking into account all the elastic scattering channels and using the deformation potentials provided in Ref. [24] (black curve); considering all the scattering channels but using our best-fit values for the deformation potentials as discussed in the text (orange curve).

when the ISB transition energy crosses the OP intravalley threshold. In these conditions, the simulated $\Delta T/T_0$ curves are sensitive to the precise value adopted for the deformation potentials, as clearly shown in the right columns of Fig. 3. In Figs 3(b), 3(d), and 3(f), we compare experimental differential transmission data for S5–S7 with numerical $\Delta T/T_0$ curves calculated: (1) setting to zero the scattering rates associated with the coupling with OPs (cyan curves); (2) using the deformation potential provided in Ref. [24] (black curves); (3) still relying on Ref. [24] for $\Xi_{\text{OP}}^{\text{intra}}$ but suppressing the electron-OP scattering rate due to intervalley events (green curves); and (4) the same as for (3) but using our best-fitting value for $\Xi_{\text{OP}}^{\text{intra}}$ (orange curve). As a first comment to these results, we notice that the characteristic decay time τ for the relaxation dynamics, inferred fitting with an exponential curve the first 30 ps of the $\Delta T/T_0$ signal, does not dramatically drop when the ISB transition energy overcomes both the OP thresholds. Indeed, we still find τ values on the order of 20–30 ps, as already obtained for the lower ISB transition energy samples. This fact confirms that thanks to the nonpolar character of group-IV lattices, the electron-phonon coupling impacts the ISB dynamics much less than what occurs in III–V-based MQW systems at comparable transition energies. Moreover, since the black and the green curves shown in Fig. 3 dramatically overestimate the $\Delta T/T_0$ decay rate, we also infer that the literature values for both the deformation potentials are not directly applicable to describe 2D Ge-based systems. In particular, the behavior of the green curves in Fig. 3 point in favor of a lower value for $\Xi_{\text{OP}}^{\text{intra}}$. On the opposite side, the underestimated decay rates associated with the cyan curves of Fig. 3 indicate that the complete suppression of the electron-OP interaction is not a realistic scenario. Note that these conclusions are not completely in line with those reported in Ref. [23] where instead a reasonable matching between numerical and experimental $\Delta T/T_0$ signals in Ge/SiGe MQWs was obtained with $\Xi_{\text{OP}}^{\text{inter}} = 0$ but still relying for $\Xi_{\text{OP}}^{\text{intra}}$ on the

value reported in Ref. [24]. This discrepancy can be attributed to the fact that elastic scattering channels were not explicitly considered in the model discussed in Ref. [23]. In fact, their role was accounted for just assuming that the L_1 and L_2 subbands were at each time step in mutual thermal equilibrium, hence introducing a common electron temperature and chemical potential. On the contrary here we use subband-dependent values for these quantities and explicitly consider the elastic scattering rates. The good agreement of the orange curves in Fig. 3 with the experimental data reported for samples S5, S6, and S7 suggests that the electron coupling with the optical branch can be described neglecting intervalley processes and assuming our best-fitting value $\Xi_{\text{OP}}^{\text{intra}} = 1.4 \times 10^8$ eV/cm.

To provide more evidence supporting our proposed value for $\Xi_{\text{OP}}^{\text{intra}}$, we measured the $\Delta T/T_0$ signal also at a larger lattice temperature and lower pumping power in order to change the relative impact of the inelastic and elastic scattering rates and the subband populations after the excitation. In the left panel of Fig. 4, we show $\Delta T/T_0$ for sample S7, recorded using a lower pump-power density with respect to the experimental conditions of panel (f) of Fig. 3. Accordingly, we observe a smaller peak value for the differential transmission signal, while the characteristic decay time τ remains nearly constant around 25 ps. In fact the L_2 - L_1 relaxation by OP emission does not need to be thermally activated, being the transition energy above the intravalley OP threshold. Also in this case, the measurement is well reproduced by the numerical simulation, obtained using our best-fit value for $\Xi_{\text{OP}}^{\text{intra}}$ (orange curve). This good agreement is preserved also when the lattice temperature is increased to 80 K (Fig. 4, right panel). In this case the experimental relaxation time reduces from (25 ± 2) to (11 ± 2) ps, due to the increased inelastic rates associated with the larger lattice temperature. It is interesting to note that the relaxation time at 80 K remains longer than 10 ps, in contrast to the subpicosecond values measured in III–V compounds in the same temperature range.

IV. CONCLUSIONS

A combined experimental and theoretical approach for the investigation of the carrier relaxation dynamics using a large set of *n*-type Ge/SiGe MQW heterostructures allowed us to estimate the effective deformation potentials governing the coupling of electrons to OP in inter- and intravalley scattering processes. Relying on a calibration procedure of a numerical model against the time-dependent differential transmission measured in single-color pump-probe experiments, we find that the electron-phonon coupling in 2D Ge/SiGe multilayer structures is less effective than that estimated in bulk Ge. In particular, we found that the ISB relaxation mediated by the emission of an OP phonon in an intervalley scattering event is suppressed. Moreover, we estimate for the defor-

mation potential governing intravalley OP scattering $\Xi_{OP}^{intra} = 1.4 \times 10^8$ eV/cm a value which represents a reduction by a factor of 4 with respect to bulk Ge. This reduced e-OP coupling is responsible for the large intersubband relaxation times (≥ 20 ps) observed in samples with the L_1 - L_2 ISB transition energy above the OP one.

ACKNOWLEDGMENTS

This work is supported by the European Union research and innovation programme Horizon 2020 under Grant No. 766719—FLASH project. For access to the FEL facility, we acknowledge the support of the project CALIPSOplus under Grant Agreement No. 730872 from the EU Framework Programme for Research and Innovation HORIZON 2020.

-
- [1] H. Sakaki, T. Noda, K. Hirakawa, M. Tanaka, and T. Matsusue, *Appl. Phys. Lett.* **51**, 1934 (1987).
- [2] S. C. Lee, I. Galbraith, and C. R. Pidgeon, *Phys. Rev. B* **52**, 1874 (1995).
- [3] H. Rucker, E. Molinari, and P. Lugli, *Phys. Rev. B* **45**, 6747 (1992).
- [4] A. Bashir, K. Gallacher, R. W. Millar, D. J. Paul, A. Ballabio, J. Frigerio, G. Isella, D. Kriegner, M. Ortolani, J. Barthel *et al.*, *J. Appl. Phys.* **123**, 035703 (2018).
- [5] T. Grange, S. Mukherjee, G. Capellini, M. Montanari, L. Persichetti, L. Di Gaspere, S. Birner, A. Attiaoui, O. Moutanabbir, M. Virgilio *et al.*, *Phys. Rev. Appl.* **13**, 044062 (2020).
- [6] C. Ciano, M. Virgilio, M. Montanari, L. Persichetti, L. Di Gaspere, M. Ortolani, L. Baldassarre, M.H. Zoellner, O. Skibitzki, G. Scalari *et al.*, *Phys. Rev. Appl.* **11**, 014003 (2019).
- [7] L. Persichetti, M. Montanari, C. Ciano, L. Di Gaspere, M. Ortolani, L. Baldassarre, M. Zoellner, S. Mukherjee, O. Moutanabbir, G. Capellini *et al.*, *Crystals* **10**, 179 (2020).
- [8] A. Sammak, D. Sabbagh, N. W. Hendrickx, M. Lodari, B. Paquelet Wuetz, A. Tosato, L. Yeoh, M. Bollani, M. Virgilio, M. A. Schubert *et al.*, *Adv. Funct. Mater.* **29**, 1807613 (2019).
- [9] N. W. Hendrickx, D. P. Franke, A. Sammak, G. Scappucci, and M. Veldhorst, *Nature (London)* **577**, 487 (2020).
- [10] M. Lodari, A. Tosato, D. Sabbagh, M. A. Schubert, G. Capellini, A. Sammak, M. Veldhorst, and G. Scappucci, *Phys. Rev. B* **100**, 041304(R) (2019).
- [11] D. J. Paul, *Laser Photonics Rev.* **4**, 610 (2010).
- [12] K. Gallacher, M. Ortolani, K. Rew, C. Ciano, L. Baldassarre, M. Virgilio, G. Scalari, J. Faist, L. Di Gaspere, M. De Seta *et al.*, *Opt. Express* **28**, 4786 (2020).
- [13] T. Grange, D. Stark, G. Scalari, J. Faist, L. Persichetti, L. Di Gaspere, M. De Seta, M. Ortolani, D. J. Paul, G. Capellini *et al.*, *Appl. Phys. Lett.* **114**, 111102 (2019).
- [14] A. Dobbie, M. Myronov, R. J. H. Morris, A. H. A. Hassan, M. J. Prest, V. A. Shah, E. H. C. Parker, T. E. Whall, and D. R. Leadley, *Appl. Phys. Lett.* **101**, 172108 (2012).
- [15] S. Cho, I. Man Kang, K. Rok Kim, B.-G. Park, and J. S. Harris, *Appl. Phys. Lett.* **103**, 222102 (2013).
- [16] L. Thumfart, J. Carrete, B. Vermeersch, N. Ye, T. Truglas, J. Feser, H. Groiss, N. Mingo, and A. Rastelli, *J. Phys. D: Appl. Phys.* **51**, 014001 (2018).
- [17] Z. Aksamija and I. Knezevic, *Phys. Rev. B* **88**, 155318 (2013).
- [18] S. Wirths, D. Buca, and S. Mantl, *Prog. Cryst. Growth Charact. Mater.* **62**, 1 (2016).
- [19] W. Pötz and P. Vogl, *Phys. Rev. B* **24**, 2025 (1981).
- [20] M. Cardona, *Light Scattering in Solids* (Springer, Berlin, 1975).
- [21] B. K. Ridley, *Quantum Processes in Semiconductors* (Clarendon, Oxford, 1988).
- [22] W. A. Harrison, *Phys. Rev.* **104**, 1281 (1956).
- [23] M. Virgilio, M. Ortolani, M. Teich, S. Winnerl, M. Helm, D. Sabbagh, G. Capellini, and M. De Seta, *Phys. Rev. B* **89**, 045311 (2014).
- [24] C. Jacoboni, F. Nava, C. Canali, and G. Ottaviani, *Phys. Rev. B* **24**, 1014 (1981).
- [25] M. V. Fischetti, *IEEE Trans. Electron Devices* **38**, 634 (1991).
- [26] M. A. Renucci, J. B. Renucci, R. Zeyher, and M. Cardona, *Phys. Rev. B* **10**, 4309 (1974).
- [27] P. B. Allen and M. Cardona, *Phys. Rev. B* **23**, 1495 (1981).
- [28] G. Sun, H. H. Cheng, J. Menéndez, J. B. Khurgin, and R. A. Soref, *Appl. Phys. Lett.* **90**, 251105 (2007).
- [29] M. De Seta, G. Capellini, M. Ortolani, M. Virgilio, G. Grosso, G. Nicotra, and P. Zaumseil, *Nanotechnology* **23**, 465708 (2012).
- [30] M. Montanari, M. Virgilio, C. L. Manganelli, P. Zaumseil, M. H. Zoellner, Y. Hou, M. A. Schubert, L. Persichetti, L. Di Gaspere, M. De Seta *et al.*, *Phys. Rev. B* **98**, 195310 (2018).
- [31] T. Ando, A. B. Fowler, and F. Stern, *Rev. Mod. Phys.* **54**, 437 (1982).
- [32] L. Bagolini, M. Montanari, L. Persichetti, L. Di Gaspere, G. Capellini, M. Ortolani, M. De Seta, and M. Virgilio, *Phys. Rev. B* **101**, 245302 (2020).
- [33] M. Virgilio, G. Grosso, G. Pizzi, M. De Seta, G. Capellini, and M. Ortolani, *Phys. Rev. B* **86**, 205317 (2012).
- [34] K. Driscoll and R. Paiella, *J. Appl. Phys.* **102**, 093103 (2007).
- [35] M. Ortolani, D. Stehr, M. Wagner, M. Helm, G. Pizzi, M. Virgilio, G. Grosso, G. Capellini, and M. De Seta, *Appl. Phys. Lett.* **99**, 201101 (2011).
- [36] A. Valavanis, PhD thesis, University of Leeds, 2009, <http://etheses.whiterose.ac.uk/1262/>.